

Article

Resonance-Enhanced Quantum Well Micropillar Array with Ultra-Narrow Bandwidth and Ultra-High Peak Quantum Efficiency

Hanxiao Shao ^{1,2,3}, Yun Xu ^{1,2,3,*}, Longfeng Lv ^{1,2,3}, Bo Cheng ^{1,2,3} and Guofeng Song ^{1,2,3}

- ¹ Institute of Semiconductors, Chinese Academy of Sciences, Beijing 100083, China; shaohanxiao@semi.ac.cn (H.S.); lflv@semi.ac.cn (L.L.); chengbo9610@semi.ac.cn (B.C.); sgf@semi.ac.cn (G.S.)
- ² College of Materials Science and Opto-Electronic Technology, University of Chinese Academy of Sciences, Beijing 100049, China
- ³ Beijing Key Laboratory of Inorganic Stretchable and Flexible Information Technology, Beijing 100083, China
- * Correspondence: xuyun@semi.ac.cn

Abstract: Infrared cameras with narrow-band detection capability are widely used for SF₆ gas detection, which is an essential part of power equipment inspection. Narrow-band detection is usually achieved by a combination of quantum well infrared photodetectors (QWIPs) and narrow-band filters. Improving the quantum efficiency of QWIPs and reducing the detection bandwidth are important ways to improve camera performance. In this study, a back-incident-type device of quantum well micropillar array targeting at a 10.5 μm central wavelength is designed and studied by three-dimensional simulation. The operating mechanism of the device was determined by investigating the effect of the device geometry on the quantum efficiency. The enhanced absorption capability of the device mainly comes from the Fabry–Pérot resonance and the antireflection effect. The final device exhibits a remarkable peak quantum efficiency of 83% at 10.5 μm and an ultra-narrow spectral bandwidth of 0.2 μm. These excellent properties are achieved without an antireflective film and narrow-band filter, which can significantly improve the narrow-band capability and integration of the system; the dark current reduces to be 0.2762 times due to the low-duty cycle. These properties indicate that the structure of the quantum well micropillar array is of great significance to the development of QWIPs used in gas detection.

Keywords: quantum well micropillar array; QWIP; 10.5 μm; SF₆ gas detection; ultra-narrow-band detection; ultra-high peak quantum efficiency; on-chip optical integration



Citation: Shao, H.; Xu, Y.; Lv, L.; Cheng, B.; Song, G. Resonance-Enhanced Quantum Well Micropillar Array with Ultra-Narrow Bandwidth and Ultra-High Peak Quantum Efficiency. *Electronics* **2022**, *11*, 1396. <https://doi.org/10.3390/electronics11091396>

Academic Editor: Antonio Di Bartolomeo

Received: 14 March 2022

Accepted: 18 April 2022

Published: 27 April 2022

Publisher's Note: MDPI stays neutral with regard to jurisdictional claims in published maps and institutional affiliations.



Copyright: © 2022 by the authors. Licensee MDPI, Basel, Switzerland. This article is an open access article distributed under the terms and conditions of the Creative Commons Attribution (CC BY) license (<https://creativecommons.org/licenses/by/4.0/>).

1. Introduction

Sulfur hexafluoride (SF₆) is a synthetic, colorless, odorless, nontoxic, and extremely inert gas. Due to its excellent insulation and arc extinguishing properties, SF₆ is widely used in power systems [1]. However, on the one hand, SF₆ has a strong greenhouse effect, and its global warming potential (GWP) is thousands of times that of carbon dioxide; on the other hand, SF₆ can produce some low-fluorine compounds of sulfur under strong arcing, which will react with water and oxygen in the air to produce highly toxic gases. Therefore, the leakage of SF₆ will create serious environmental problems and harm human health. SF₆ gas detection is an essential part of power equipment inspection. SF₆ gas has a narrow absorption band in the long-wave infrared (LWIR) band and peaks near 10.5 μm. This narrow band absorption places stringent demands on the photodetectors, as they need to have high quantum efficiency in this limited spectral range to maintain high sensitivity. Thanks to highly mature GaAs/AlGaAs material techniques, quantum well infrared photodetectors (QWIP) are highly reproducible, and their performance can be accurately predicted by physical laws. For QWIPs, the peak response wavelength can be

designed precisely and can cover the mid-wave infrared, long-wave infrared, very long-wave infrared, and terahertz bands [2,3]. The spectral bandwidth can be tuned from narrow ($\Delta\lambda/\lambda \sim 10\%$) to wide ($\Delta\lambda/\lambda \sim 40\%$) according to application requirements [4], and $\Delta\lambda$ is the full width at half maximum (FWHM) of the response spectrum. These features provide QWIPs with unique advantages in gas detection. IRnova AB, U.S. Army Research Laboratory, and the Institute of Shanghai Technical Physics have designed and fabricated QWIPs targeting at 10.5 μm central wavelength for gas detector [5–8].

Despite the obvious advantages, the low quantum efficiency is the main factor limiting QWIP's performance. Specialized optical modulation structures need to be designed to meet the unique requirement of QWIPs for vertically polarized light. Current researchers usually design grating-type QWIP structures [9–13] or corrugated QWIP structures [14,15] to meet the conditions for the absorption of normal incident light by QWIPs. However, the low efficiency of optical coupling dramatically limits the sensitivity of the device. Products marked 640-SF6 of IRnova AB have a peak conversion efficiency (CE) of 1.3% at 10.5 μm and a spectral bandwidth of 0.5 μm (10.3–10.8 μm) [7]. There are two reasons for the low conversion efficiency: (1) the low efficiency of optical coupling; (2) the use of narrow-band filters. Since the spectral bandwidth of the device ($\Delta\lambda \sim 1 \mu\text{m}$ for 10.5 μm) is much larger than the absorption bandwidth of the SF6 gas ($\sim 0.1 \mu\text{m}$), the narrow-band filters need to be used to increase the contrast of targets at the cost of signal loss and reduced system integration. K.K. Choi proposed an electromagnetic model for QWIPs [16–18]. Based on this model, they designed resonator-QWIPs with the peak absorption quantum efficiency (QE) of 29.4% and the peak CE of 20.2% for SF6 gas sensor applications [6]. In addition, researchers have designed different structures, such as the structures of the metasurface [19], metal-semiconductor microcavity [20,21], and high-efficiency coupling grating [21], to overcome the low quantum efficiency of quantum well devices.

Our previous work [22] found that the nanowire-array-UTC-PD can have a powerful optical absorption at 1064 nm at a thin active layer thickness due to the Fabry–Pérot-like resonance effect. If this feature can be ported to QWIPs, the thin active layer means high conductivity gain, which improves the signal-to-noise ratio. Since the surface dark current component of the QWIP is almost negligible, the low duty cycle of the micropillar array facilitates the reduction of dark current. More importantly, the quantum well micropillar array can act as a subwavelength structure to couple normal incident light. It seems that the structure of the quantum well micropillar array is promising for FPA-level applications. Researchers have developed research around the quantum well micropillar array. In 2017, Mohammad Karimi reported broadband nanowire heterostructure array photodetectors exhibiting a photo-response from 3–20 μm waveband excited by intersubband transitions in low-bandgap InAsP quantum discs within InP nanowires under normal incidence [23]. In 2020, YE Xin-Hui designed a quantum well subwavelength micropillar array structure targeting at the 8.7 μm central wavelength [24]. The above works demonstrate the absorption of the quantum well micropillar array for vertically incident light. However, the working mechanism of the structure under backward incidence has not been investigated, so whether it can be applied to the focal plane array (FPA) is uncertain.

This study designed a quantum well micropillar array with a high peak QE and narrow detection half-height width targeting at 10.5 μm central wavelength. In Section 2, models of this optoelectronic simulation are introduced. In Section 3.1, we explore the working mechanism of the quantum well micropillar array under back incidence based on the structure in [24]. The simulation results show that the structure is suitable for FPA application. In Section 3.2, we designed a resonance-enhanced quantum well micropillar array with an antireflection effect targeting at 10.5 μm central wavelength for SF6 gas detection, and the mechanism of the enhanced optical absorption effect is discussed. Finally, a device of high peak quantum efficiency of 83% at 10.5 μm and ultra-narrow spectral bandwidth of 0.2 μm is obtained without antireflective film and filters.

2. Physical Model

For QWIP, the absorption quantum efficiency, labeled as QE, is given by [17]

$$\begin{aligned} \text{QE} &= \frac{1}{P_0} \int_V dI(\vec{r}), \\ &= \frac{1}{P_0} \int_V \alpha I(\vec{r}) d^3r, \\ &= \frac{\alpha}{A \frac{c \epsilon_0}{2} E_0^2} \int_V \frac{nc\epsilon_0}{2} |E_z(\vec{r})|^2 d^3r, \\ &= \frac{n\alpha}{AE_0^2} \int_V |E_z(\vec{r})|^2 d^3r \end{aligned} \quad (1)$$

where P_0 is the normally incident optical power, I is the optical intensity associated with E_z , α is the absorption coefficient of the active region, A is the area of the incident light source, V is the detector active volume, E_0 is the electric field intensity of the incident light, n is the material refractive index, ϵ_0 is dielectric constant, and c is the speed of light. The electromagnetic field profile $E_z(\vec{r})$ is calculated by solving the Maxwell equation through the finite element method using the software Comsol Multiphysics. The simulation domain space is curtailed by setting the floquet periodic boundary conditions in the horizontal direction. The reflection modes in the vertical direction are suppressed using the perfect matching layer. The polarization and power of the incident light are introduced by setting the boundary conditions of the port. The calculated $E_z(\vec{r})$ in the active region is integrated and then brought into the Equation (1) to obtain the quantum efficiency of the device.

The absorption coefficient (α) of active region can be described as

$$\alpha(\hbar\omega) = \int_E^\infty g(E_{ij}) L(\hbar\omega - E_{ij}) dE_{ij}, \quad (2)$$

where \hbar is the reduced Planck constant, ω is angle frequency of the incident light, $g(E_{ij})$ is the local gain due to a transition from the energy level labeled as i to the energy level labeled as j , and $L(\hbar\omega - E_{ij})$ is the line-shape function of the gain broadening model. The commercial software Crosslight Apsys is used to calculate α in this paper. The single quantum well period is modeled, and an infinitely high potential barrier is set at 100 nm from the GaAs layer as a boundary condition. By solving Schrödinger's equation, the density of states, energy level positions, and wave functions of the ground and excited states are obtained to calculate $g(E_{ij})$. The Lorentzian gain broadening model is used, so $L(\hbar\omega - E_{ij})$ can be described as

$$L(\hbar\omega - E_{ij}) = \frac{1}{\pi} \frac{\hbar/\tau_{in}}{(\hbar\omega - E_j - E_i)^2 + (\hbar/\tau_{in})^2} \quad (3)$$

where \hbar/τ_{in} is broadening factor.

In order to ensure the accuracy of the models, we performed a re-simulation of the absorption coefficient of the structures in [25] using Crosslight Apsys, and we performed simulation replication of a quantum grid infrared spectrometer in [18] and a top incidence-type quantum well subwavelength micropillar array structure reported in [24] using Comsol Multiphysics. The re-simulated results are consistent with those in the literature.

3. Results

3.1. Operating Mechanism of Quantum Well Micropillar Array under the Back Incidence

In this subsection, we first explore the operation mechanism of the back-incidence quantum well micropillar array based on the structure in [24]. The geometric design of the device is composed of the vertical micropillar array on the public GaAs N-contact layer (blue pattern) and GaAs substrate (dark grey pattern), as shown in Figure 1a. The vertical micropillar comprises upper and lower GaAs contact layers (blue pattern) and active region (green pattern). The material in the gap of the micropillar is Benzo-cyclobutane (BCB). A total of 200 nm Au is placed on the top of the N-contact layer as an upper electrode.

As shown in Figure 1b, the light source is applied to the bottom of the device, and the periodic boundary conditions are set for the unit. As shown in Figure 1c, the top GaAs contact layer thickness (h_{n1}) is set to be $1.1 \mu\text{m}$; the absorber layer thickness (h_{ab}) is set to be $2.77 \mu\text{m}$; the height (H) and the diameter (D) of the micropillar are set to $4 \mu\text{m}$ and $2.2 \mu\text{m}$, respectively; and the unit's period (P) is set to be $4 \mu\text{m}$. We focused on the effect of the micropillar's diameter (D) and height (H), and the unit's period (P) on the QE, which is calculated by Equation (1). To assess the light-coupling efficiency of different detector geometries, we first assume a constant $\alpha = 0.1 \mu\text{m}^{-1}$ independent of wavelengths. This α is the typical peak value for a QWIP material with $1 \times 10^{18} \text{cm}^{-3}$ doping [16].

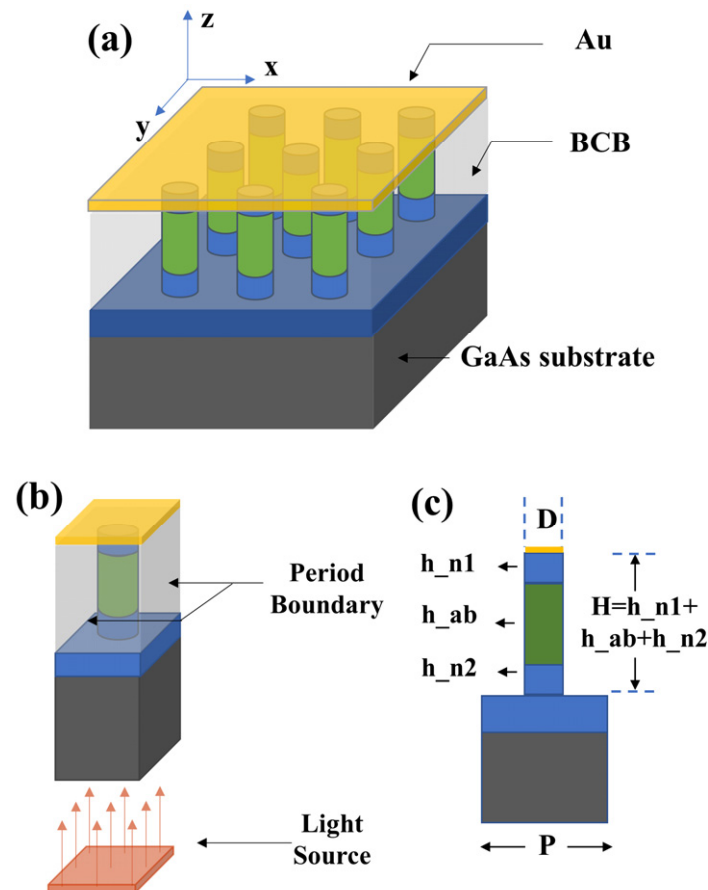


Figure 1. Geometric structures of (a) quantum well micropillar array, (b) periodic unit, and (c) XZ cross-section of the periodic unit.

Figure 2a shows the QE of the periodic unit with different micropillar diameters versus the incident wavelength. This light coupling scheme is similar to the multipole scattering from the individual metal strips [26]. The maximum coupling efficiency needs to meet the condition described as $\lambda = 2n_{eff} \cdot D/N$, where λ is the incident wavelength, D is the diameter of the micropillar, n_{eff} is the effective refractive index, and N is an odd integer. It is clear that, as the diameter increases, the peak wavelength is red-shifted, and the spacing between the two peak wavelengths at the same diameter becomes progressively more prominent. Figure 2b shows the QE of the periodic unit with different periods versus the incident wavelength. Peak wavelength is not sensitive to the period (P). We guess the shift in the peak wavelength is due to the change in the effective refractive index. The micropillar and BCB form the scattering unit with the effective refractive index n_{eff} . When the diameter remains constant and the period is changed, the change in the volume of the low-refractive-index BCB causes only a slight effect on the effective refractive index leading to a slight shift of the peak wavelength.

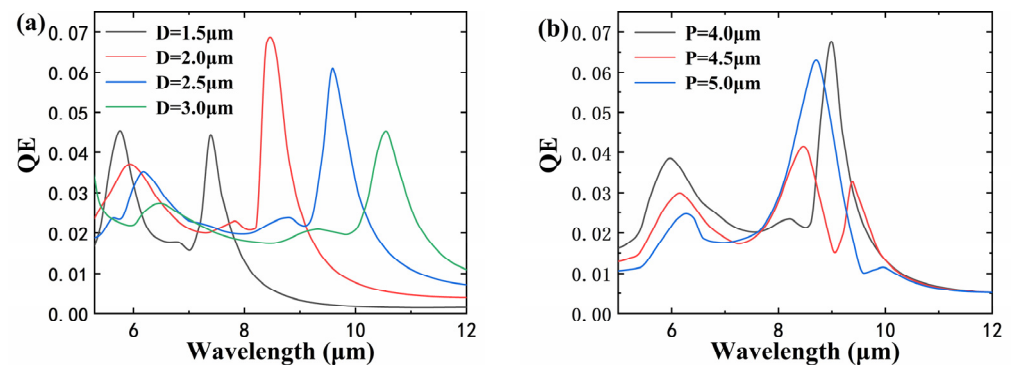


Figure 2. QE as a function of incident wavelength (a) at different micropillar diameters and (b) at different unit periods.

Figure 3a shows the QE of the periodic unit with different micropillar heights (H) versus the incident wavelength. There are two peaks from 5 to 12 μm at different H . The left peak wavelength is red-shifted with increasing H . This phenomenon is consistent with the fundamental grating scattering law, which can be described as $H = m \frac{\lambda_p}{4n_{\text{grating}}}$, $m = 1, 3, 5, \dots$, where H is the grating groove depth, λ_p is the peak wavelength, and n_{grating} is the refractive index [4]. The right peaks are almost stable near 8.5 μm at different H . We think this peak arises from the multipole scattering effect mentioned in the previous paragraph. Figure 3b shows the QE of the periodic unit with the same micropillar height (H) but different h_{ab} versus incident wavelength. When H remains constant, the peak wavelength does not shift with the thickness of the absorption region (h_{ab}), only the QE increases.

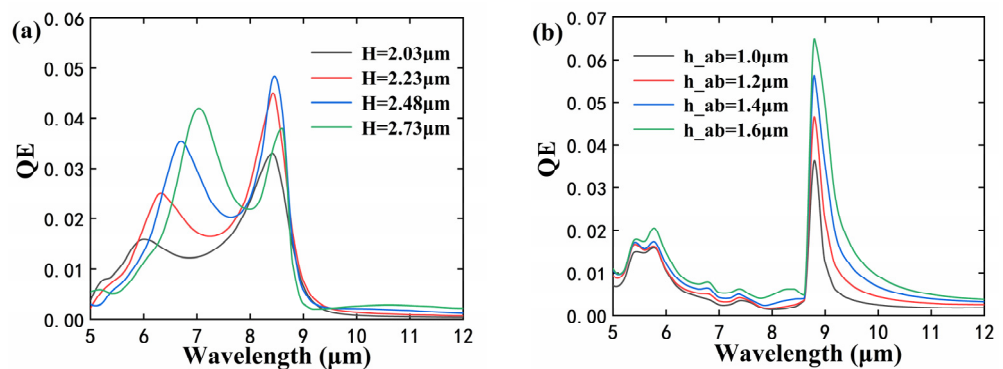


Figure 3. (a) QE as a function of incident wavelength at different micropillar heights. h_{n1} and h_{n2} remain constant at 1.1 μm and 0.13 μm , respectively. The micropillar height (H) changes with h_{ab} . (b) QE as a function of incident wavelength at different h_{ab} . The micropillar height (H) remains constant at 4 μm , only h_{ab} changes.

From the above simulation results, we obtain the operation mechanism of the quantum well micropillar array in the back-incidence case. In the long-wave infrared band (8–12 μm), the maximum coupling efficiency depends mainly on the diameter of the micropillar. The overall coupling efficiency of this scheme is low. However, considering a large amount of incident light reflection at the air–substrate interface, if antireflection films can be added to the device, it is promising to increase the value of QE to nearly 20%, which is acceptable for QWIP-FPA.

3.2. Quantum Well Micropillar Array with Resonance-Enhanced and Antireflection Effects Targeting at 10.5 μm Central Wavelength

Figure 4a shows the optical path of the device in Section 3.1. In the z -direction, there is no cavity effect within region 2 and region 3 due to the thick substrate. The incident light is greatly reflected at interface 1 and interface 2, which leads to the low coupling efficiency.

We expect to introduce an FP cavity to the device to achieve high QE. As shown in Figure 4b, the cavity is designed to be composed of region 1 (low refractive index), region 2 (high refractive index), and region 3 (low refractive index). By precisely tuning the cavity size, the optical power can localize in region 2, and the public GaAs contact layer is expected to work as an antireflective film to minimize reflection at interface 1.

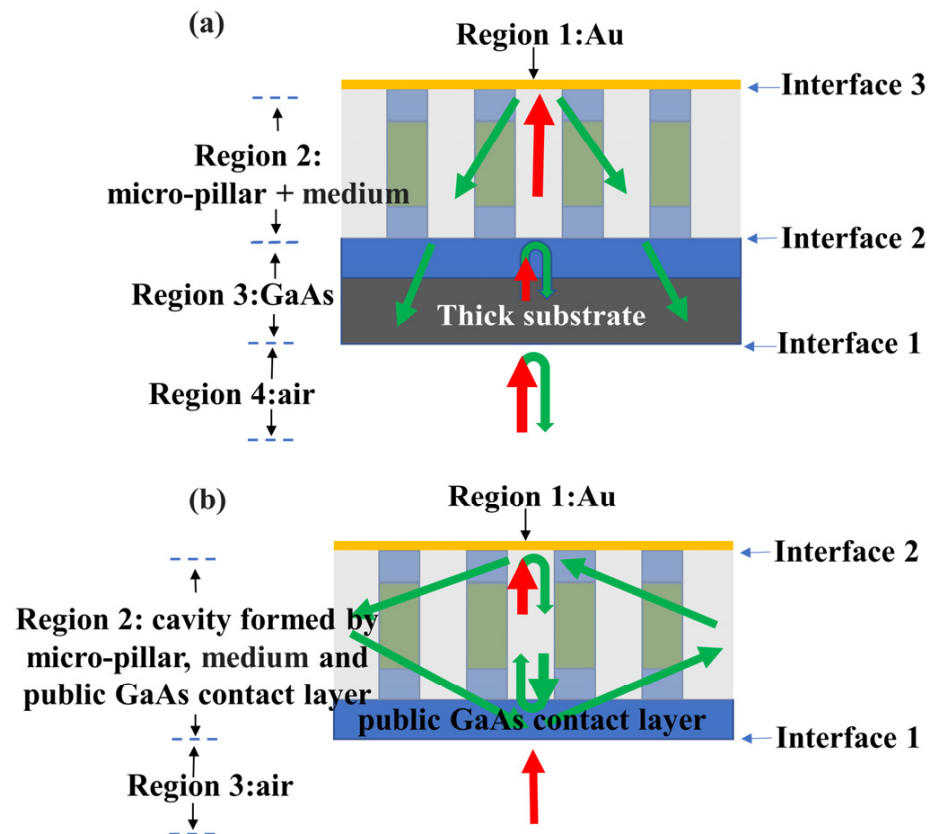


Figure 4. The optical path of (a) quantum well micropillar array with a thick substrate, (b) quantum well micropillar array with resonance-enhanced and antireflection effects.

This subsection focuses on designing a high-quantum-efficiency quantum well micropillar array under back incidence targeting at $10.5 \mu\text{m}$ central wavelength. To obtain the operation mechanism of the device, we studied the effect of the micropillars diameter (D), the active layer thickness of (h_{ab}), and the thickness of the public GaAs contact layer (h_{public}) on QE. After scanning the parameters, we found ultra-high QE of 80% at the $10.5 \mu\text{m}$ wavelength with $D = 3.5 \mu\text{m}$, $P = 5.9 \mu\text{m}$, $h_{ab} = 1.705 \mu\text{m}$, and $h_{public} = 1.65 \mu\text{m}$. Considering the expected FP cavity effect and the antireflection effect are likely to be sensitive to the geometric parameters in the z -direction, we first investigated the impact of h_{public} and h_{ab} on the QE at $10.5 \mu\text{m}$.

Figure 5a shows the geometric model discussed in this subsection. Compared to Figure 1, the substrate is removed. We selected ZnS as the medium around the micropillar due to its weak absorption at $10.5 \mu\text{m}$ waveband and a good passivation effect for infrared detectors. The light source is applied to the bottom of the device, and periodic boundary conditions are set for the unit. As shown in Figure 5b, 200 nm Au is placed on the top of the N-contact layer as an upper electrode; h_{n1} and h_{n2} are set to be a constant of $0.5 \mu\text{m}$. To assess the light-coupling efficiency of different detector geometries, we also assume a constant $\alpha = 0.1 \mu\text{m}^{-1}$ independent of wavelengths.

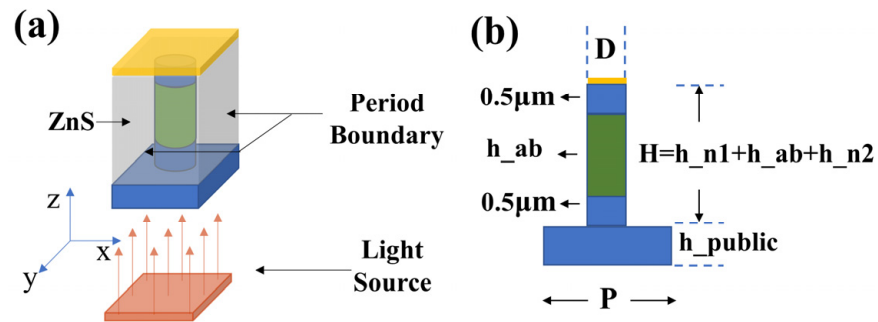


Figure 5. Geometric structures of (a) periodic unit and (b) XZ cross-section of the periodic unit.

After precise scanning of the parameters, the maximum quantum efficiency of 80% at 10.5 μm occurs at $h_{ab} = 1.705 \mu\text{m}$ and $h_{public} = 1.65 \mu\text{m}$, as shown in Figure 6a,b. In order to obtain the reasons for the high quantum efficiency at 10.5 μm, we have analyzed $|E_x|$ distribution in XZ cross-sections of the device at several points in Figure 6b. As shown in Figure 6c, in the air region, the nonuniformity of $|E_x|$ distribution near the interface 1 arises from the leakage of the mode excited by the grating; the bright and dark distribution of the far-field mainly stems from the interference between the incident light and the light reflected at the interface 1. In increasing h_{ab} , the interference effect in the air region becomes weaker and then stronger. When h_{ab} is equal to 1705 nm, the interference effect almost disappeared, indicating almost no light reflection at interface 1. This phenomenon suggests that the device may work as an antireflective film. The best antireflection effect occurs at $L = \frac{\lambda}{4 \times n}$ [27,28], where λ is the wavelength, and L and n are the film's thickness and effective refractive index, respectively. Before the increase in h_{ab} to 1705 nm, the device has an excellent energy limiting effect. It suggests that the peak quantum efficiency of 80% arises from the device with $h_{ab} = 1705 \text{ nm}$ working as an FP cavity in the z-direction. During the increase of h_{ab} from 1705 nm to 2098 nm, the mode leakage becomes more severe. As the cavity length changes from the optimal value, the energy localization condition is increasingly unsatisfied, decreasing the quantum efficiency.

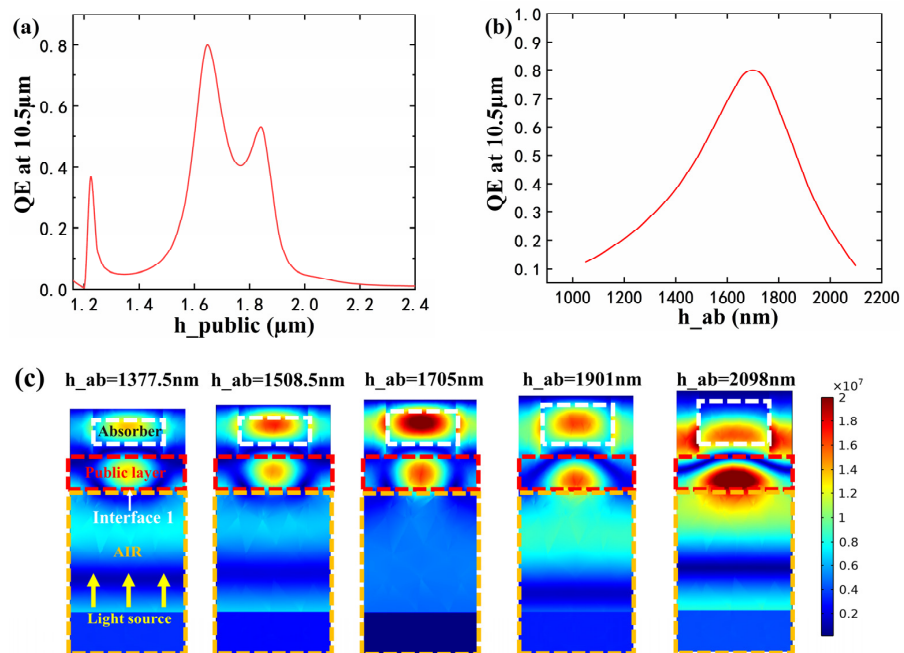


Figure 6. (a) QE at 10.5 μm as a function of h_{public} . (b) QE at 10.5 μm as a function of h_{ab} . (c) $|E_x|$ distribution in XZ cross-sections of the device at $h_{ab} = 1377.5 \text{ nm}$, 1508.5 nm, 1705 nm, 1901 nm, and 2098 nm in Figure 6b.

Figure 7a shows QE at different micropillar diameters (D) versus the incident wavelength. As D increases, the peak wavelength red-shifts. This shift seems to be consistent with the effect of the multipole scattering mentioned above. As a comparison, Figure 7b shows the QE of the device with a thick substrate, and no peak wavelength appears between 10 and 13 μm , so the role of the multipole scattering effect is excluded. We guess that the antireflection effect mentioned above can explain the shift of the peak wavelength with D . As D increases, the volume share of the high-refractive-index micropillar increases, which leads to the increase of the antireflective film's effective refractive index; if the L remains constant, the peak wavelength will be red-shifted.

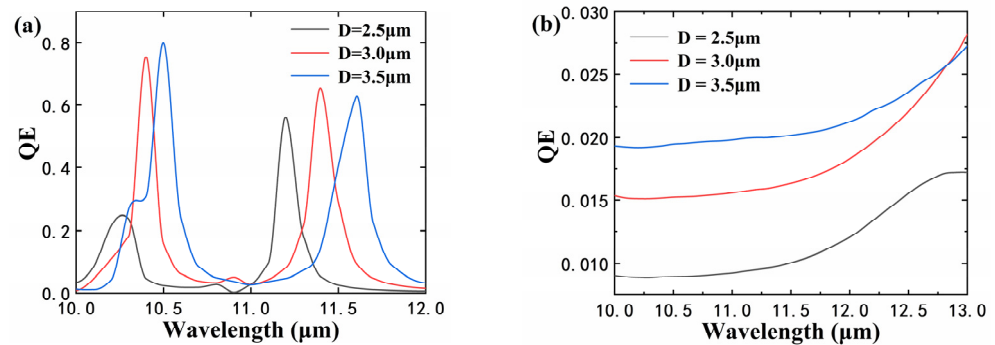


Figure 7. (a) QE as a function of incident wavelength at different micropillar diameters (D). The substrate is removed, and cavity effects appear by tuning the device sizes, so the peak QE is a remarkable value for QWIP. (b) QE as a function of incident wavelength at different micropillar diameters (D). For comparison, a thick substrate is added to the simulation in this figure. The device exhibits a very low QE due to the absence of cavity effects. h_{ab} and h_{public} are set to be the optimal value of 1.705 μm and 1.65 μm , respectively.

To better define the operating mechanism of the device, we analyzed the $|E_x|$ distribution in XZ cross-sections of the device at 10.1 μm , 10.5 μm , and 10.9 μm of the blue line in Figure 7a. The $|E_x|$ distribution in Figure 8b shows that the structure achieves both good antireflection and sound energy localization effects for 10.5 μm . As shown in Figure 8a,c, both effects are weakened as the wavelength changes.

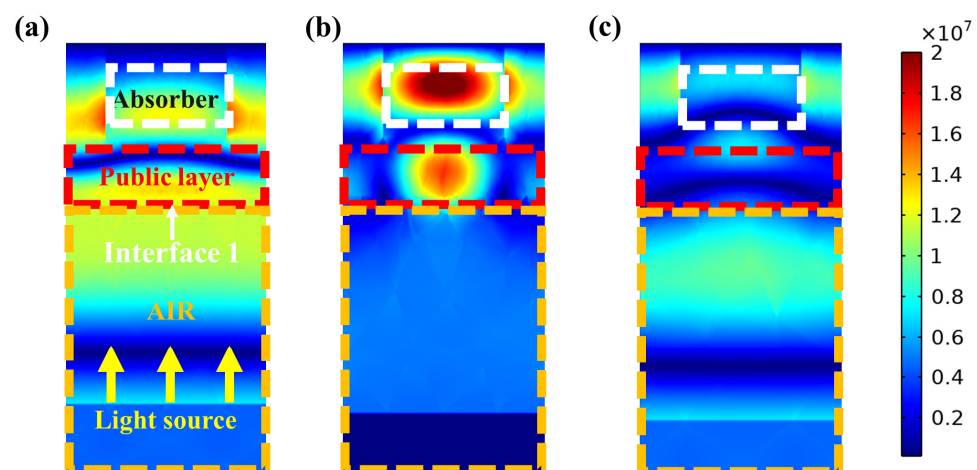


Figure 8. $|E_x|$ distribution in XZ cross-sections of the device at (a) 10.1 μm , (b) 10.5 μm , and (c) 10.9 μm of the blue line in Figure 7a.

3.3. Performance of the Final Device

Finally, we designed the dimensions of the device as $D = 3.5\mu\text{m}$, $P = 5.9\mu\text{m}$, $h_{\text{ab}} = 1.705\mu\text{m}$, and $h_{\text{public}} = 1.65\mu\text{m}$. Material of the active region consists of 26 periods of 56 \AA GaAs/600 \AA $\text{Al}_{0.2}\text{Ga}_{0.8}\text{As}$. The software Crosslight Apsys is used to calculate the absorption

spectrum of the active region. Figure 9 shows the simulation results with different doping concentrations in the well. The absorption spectrum is taken into the software Comsol Multiphysics for the QE calculation of the final device.

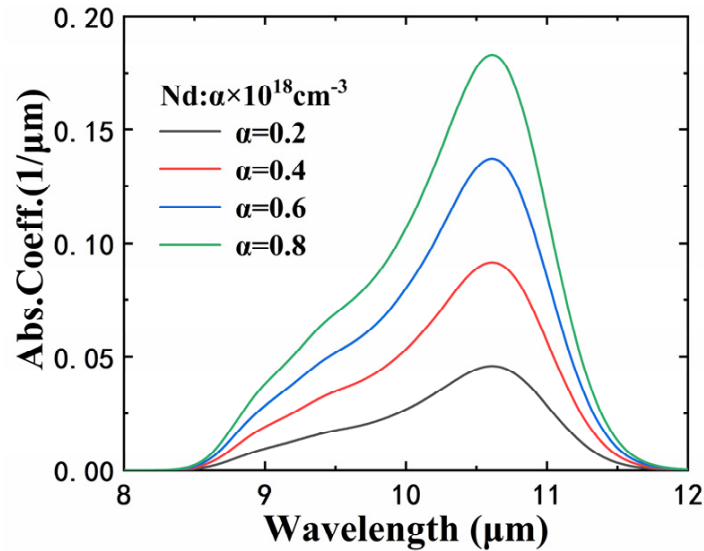


Figure 9. The absorption coefficient at different doping concentrations in the well versus wavelength.

Figure 10a shows the QE spectrum of the device with different doping concentrations in well. QE peaks at 10.5 μm. The peak QE saturates with increasing doping concentration, reaching a maximum of 83%. The spectral bandwidth at different doping concentrations is more diminutive than 0.2 μm. Figure 10b shows the dark current density at different doping concentrations versus the bias voltage. Dark current increases by orders of magnitude with the increasing doping concentration, which is consistent with the findings in [29]. For FPA, a small ratio of dark current to QE should be chosen to reduce the noise equivalent temperature difference (NETD). NETD can be described as $NETD = \left\{ \frac{1}{C} \left(\frac{N_{FPA}}{N_{tot}} \right) \right\} \left(1 + \frac{I_{dark}}{I_{ph}} \right)$, where C is the contrast of the detection waveband, N_{FPA} is the total number of noise electrons of FPA, N_{tot} is the total number of electrons integrated by read-out-integrated-circuit (ROIC), I_{dark} is the dark current of the detector, and I_{ph} is the photocurrent excited by the background radiation, which is proportional to QE [30]. A doping concentration of $0.2 \times 10^{18} \text{ cm}^{-3}$ may be more beneficial for high-quality imaging. In addition, due to the mature passivation process of QWIP, the sidewall dark current is almost negligible compared to the bulk dark current, so the actual dark current density of this device should be multiplied by 0.2762 (duty cycle of the micropillar), which is also beneficial for NETD reduction.

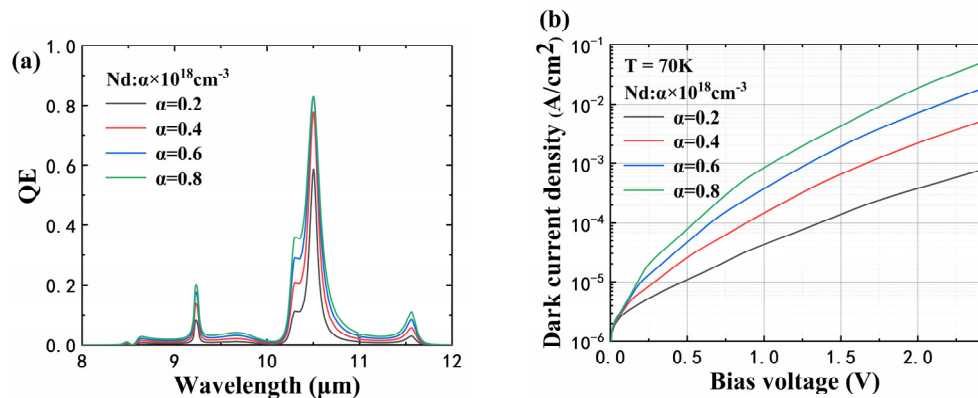


Figure 10. (a) QE of the final device with different doping concentrations in the well as a function of wavelength, (b) bulk dark current density of the final device as a function of voltage.

The comparison of the quantum well micropillar array and QWIPs reported in [5–7] is shown in Table 1. In reference [6], the conductivity gain is 0.687 for 15 periods of 56 Å GaAs/600 Å Al_{0.2}Ga_{0.8}As, and it is mentioned that narrow-band filters are necessary for SF₆ gas detection, which results in a reduction in QE. In this paper, the conductivity gain of 26 periods is calculated to be 0.404 according to the equation described as $g = \frac{g_1}{N_W}$ [31], where g_1 is the photoconductive gain for one quantum well, N_W is the number of the quantum well period; the quantum well micropillar array exhibits the best peak conversion efficiency of 0.236. The ultra-narrow spectral bandwidth of 0.15 μm significantly increases the contrast of the SF₆ gas to reduce the NETD, which allow the device to operate at higher temperatures. These properties are achieved without optical filters and antireflection films, which can significantly reduce the cost and increase the integration of the system.

Table 1. Comparison among Quantum Well Micropillar Array and QWIPs in [5–7].

| Data | [3] | [4] | [2] | This Paper |
|---|---------|---------|----------|------------|
| Peak wavelength | 10.6 μm | 10.5 μm | 10.55 μm | 10.5 μm |
| Peak QE | 0.26 | / | / | 0.585 |
| Peak CE | 0.178 | 0.013 | / | 0.236 |
| Doping concentration in well ($\times 10^{18} \text{ cm}^{-3}$) | 0.2 | / | 0.25 | 0.2 |
| Bandwidth | 0.4 μm | 0.5 μm | 1 μm | 0.15 μm |
| Optics filter | yes | yes | no | no |
| Antireflective film | no | / | yes | no |

4. Conclusions

This paper investigates the operating mechanism of the quantum well micropillar array under back incidence. The simulation results show that the structure supports the absorption of vertically incident light and is therefore suitable for FPA. For the device with a thick substrate, the peak wavelength is mainly determined by the diameter of the micropillar under the multipole scattering effect. By removing the substrate and precisely tuning the device size, the structure exhibits the excellent narrow-band detection capability without the antireflective film and narrow-band filter, significantly improving the system integration and reducing the process difficulty. With Fabry–Pérot (FP) resonance and antireflection effects, the final device exhibits a remarkable peak quantum efficiency of 83% at 10.5 μm and an ultra-narrow spectral bandwidth of 0.2 μm; the dark current can reduce to be 0.2762 times due to the low-duty cycle. This work suggests that the application of quantum well micropillar array is promising in SF₆ gas detection.

Author Contributions: Conceptualization, H.S. and Y.X.; methodology, H.S. and Y.X.; software, H.S., B.C.; validation, H.S., B.C. and L.L.; formal analysis, H.S., B.C. and L.L.; investigation, H.S.; resources, Y.X. and G.S.; data curation, H.S., L.L.; writing—original draft preparation, H.S.; writing—review and editing, Y.X., G.S. and L.L.; visualization, H.S. and L.L.; supervision, Y.X. and G.S.; project administration, Y.X. and G.S.; funding acquisition, Y.X. and G.S. All authors have read and agreed to the published version of the manuscript.

Funding: This work was supported by the National Key Research and Development Plan (no. 2020YFB2206103), the National Natural Science Foundation of China (grant no. 12075244), the Strategic Priority Research Program of Chinese Academy of Sciences (grant no. XDB43010000), the National Science and Technology Major Project (2018ZX01005101-010), the National Basic Research Program of China (973 Program) (no. 2015CB351902), the National Natural Science Foundation of China (grant no. 61835011), the National Natural Science Foundation of China (grant no. U1431231), and the Beijing Science and Technology Projects (grant no. Z151100001615042), Key Research Projects of the Frontier Science of the Chinese Academy of Sciences (no. QYZDY-SSW-JSC004).

Data Availability Statement: The simulation parameters in this study are available in Physical Properties of III-V Semiconductor Compounds, John Wiley & Sons Inc.: New Jersey, USA, 1992.

Acknowledgments: The authors would like to thank the reviewers for their helpful comments and criticism.

Conflicts of Interest: The authors declare no conflict of interest.

References

1. Zhang, X.; Zhang, Y.; Tang, J.; Cui, Z.; Li, Y.; Zhou, H.; Zhang, G.; Yang, J. Optical technology for detecting the decomposition products of SF₆: A review. *Opt. Eng.* **2018**, *57*, 110901. [[CrossRef](#)]
2. Bai, X.; Bai, P.; Li, X.; Huang, S.; Lian, X.; Song, W.; Shi, Z.; Shen, W.; Zhang, Y. Optical coupling enhancement of multi-color terahertz quantum well detector. *J. Appl. Phys.* **2021**, *130*, 203102. [[CrossRef](#)]
3. Shao, D.; Fu, Z.; Tan, Z.; Wang, C.; Qiu, F.; Gu, L.; Wan, W.; Cao, J. Research Progress on Terahertz Quantum-Well Photodetector and Its Application. *Front. Phys.* **2021**, *9*, 581. [[CrossRef](#)]
4. Soibel, A.; Bandara, S.V.; Ting, D.Z.; Liu, J.K.; Mumolo, J.M.; Rafol, S.B.; Johnson, W.R.; Wilson, D.W.; Gunapala, S.D. A super-pixel QWIP focal plane array for imaging multiple waveband temperature sensor. *Infrared Phys. Technol.* **2009**, *52*, 403–407. [[CrossRef](#)]
5. Xiangyang, L.; Ning, L.; Jintong, X.; Kaihui, C.; Guoqing, X.; Ling, W.; Yan, Z.; Longyuan, Z.; Jiqiang, W.; Wei, L. GaAs/AlGaAs QWIP IRFPA for 10.55 μm long wavelength. *Infrared Laser Eng.* **2020**, *49*, 6.
6. Engelmann, S.U.; Wise, R.S.; Sun, J.; Choi, K.K.; DeCuir, E.A.; Olver, K.A.; Fu, R.X. Design and fabrication of resonator-QWIP for SF₆ gas sensor application. In Proceedings of the Advanced Etch Technology for Nanopatterning VI, San Jose, CA, USA, 26 February–2 March 2017.
7. Smuk, S.; Ivanov, R.; Evans, D.; Sehlín, S.; Diel, W.; Hellström, S.; Höglund, L.; Smuk, A.; Costard, E.; Fulop, G.F.; et al. QWIPs are keeping their promises. In Proceedings of the Infrared Technology and Applications XLV, Baltimore, MD, USA, 14–18 April 2019.
8. Ivanov, R.; Evans, D.; Smuk, S.; Diel, W.; Rihtnesberg, D.; Höglund, L.; Gulde, M.; Costard, E.; Fulop, G.F.; Kimata, M.; et al. QWIP as solution for mobile VLWIR imaging systems. In Proceedings of the Infrared Technology and Applications XLVII, Online, 12–16 April 2021.
9. Kim, H.; Ahn, S.-Y.; Wasilewski, Z. Fabrication of grating coupled GaAs/AlGaAs quantum well infrared photodetector on an Si substrate. *J. Vac. Sci. Technol. B* **2019**, *37*, 031209. [[CrossRef](#)]
10. Hainey, M.F.; Mano, T.; Kasaya, T.; Jimba, Y.; Miyazaki, H.; Ochiai, T.; Osato, H.; Watanabe, K.; Sugimoto, Y.; Kawazu, T.; et al. Patchwork metasurface quantum well photodetectors with broadened photoresponse. *Opt. Express* **2021**, *29*, 59–69. [[CrossRef](#)]
11. Hainey, M.F.; Mano, T.; Kasaya, T.; Ochiai, T.; Osato, H.; Watanabe, K.; Sugimoto, Y.; Kawazu, T.; Arai, Y.; Shigetou, A.; et al. Near-field resonant photon sorting applied: Dual-band metasurface quantum well infrared photodetectors for gas sensing. *Nanophotonics* **2020**, *9*, 4775–4784. [[CrossRef](#)]
12. Chu, Z.; Zhou, Y.; Zhou, J.; Chen, P.; Li, Z.; Lu, W.; Chen, X. Quantum well infrared detectors enhanced by faceted plasmonic cavities. *Infrared Phys. Technol.* **2021**, *116*, 103746. [[CrossRef](#)]
13. Liang, B.W.; Huang, C.C.; Chao, S.P.; Kao, K.J.; Simbulan, K.B.; Lan, Y.W.; Kuan, C.H. Responsivity and detectivity enhancements by graphene overlay on normal-incident multicolor quantum grid infrared photodetectors. *Opt. Express* **2020**, *28*, 2456–2465. [[CrossRef](#)]
14. Goldberg, A.; Choi, K.K.; Cho, E.; McQuiston, B. Laboratory and field performance of megapixel QWIP focal plane arrays. *Infrared Phys. Technol.* **2005**, *47*, 91–105. [[CrossRef](#)]
15. Jhabvala, M.; Choi, K.K.; Monroy, C.; La, A. Development of a 1K \times 1K, 8–12 μm QWIP array. *Infrared Phys. Technol.* **2007**, *50*, 234–239. [[CrossRef](#)]
16. Andresen, B.F.; Choi, K.K.; Fulop, G.F.; Jhabvala, M.D.; Forrai, D.P.; Norton, P.R.; Waczynski, A.; Sun, J.; Jones, R. Electromagnetic modeling of QWIP FPA pixels. In Proceedings of the Infrared Technology and Applications XXXVII, Orlando, FL, USA, 25–29 April 2011.
17. Choi, K.-K.; Jhabvala, M.D.; Forrai, D.P.; Waczynski, A.; Sun, J.; Jones, R. Electromagnetic Modeling of Quantum Well Infrared Photodetectors. *IEEE J. Quantum Electron.* **2012**, *48*, 384–393. [[CrossRef](#)]
18. Kwong-Kit, C.; Jhabvala, M.D.; Forrai, D.P.; Waczynski, A.; Sun, J.; Jones, R. Electromagnetic Modeling and Design of Quantum Well Infrared Photodetectors. *IEEE J. Sel. Top. Quantum Electron.* **2013**, *19*, 1–10. [[CrossRef](#)]
19. Hainey, M.F.; Mano, T.; Kasaya, T.; Jimba, Y.; Miyazaki, H.; Ochiai, T.; Osato, H.; Sugimoto, Y.; Kawazu, T.; Shigetou, A.; et al. Breaking the interband detectivity limit with metasurface multi-quantum-well infrared photodetectors. *Opt. Express* **2021**, *29*, 43598–43611. [[CrossRef](#)]
20. Yang, K.; Ni, B.; Ge, H.; Zhang, L.; Yang, L.; Ni, H.; Tai, G.; Chang, J. A high-performance quantum well infrared photodetector based on semiconductor–metal periodic microstructure. *Opt. Quantum Electron.* **2021**, *53*, 160. [[CrossRef](#)]
21. Liu, L.; Chen, Y.; Huang, Z.; Du, W.; Zhan, P.; Wang, Z. Highly efficient metallic optical incouplers for quantum well infrared photodetectors. *Sci. Rep.* **2016**, *6*, 30414. [[CrossRef](#)]
22. Shao, H.; Cheng, B.; Xu, Y.; Song, G. Ultrahigh-quantum-efficiency and high-bandwidth nanowire array UTC-PDs working at 1064 nm. *Opt. Quantum Electron.* **2022**, *54*, 15. [[CrossRef](#)]

23. Karimi, M.; Heurlin, M.; Limpert, S.; Jain, V.; Zeng, X.; Geijselaers, I.; Nowzari, A.; Fu, Y.; Samuelson, L.; Linke, H. Intersubband Quantum Disc-in-Nanowire Photodetectors with Normal-Incidence Response in the Long-Wavelength Infrared. *Nano Lett.* **2017**, *18*, 365–372. [[CrossRef](#)]
24. Xin-Hui, Y.; Tian, X.; Hui, X.; Xi-ren, C.; Ju-Zhu, L. Quantum well micropillar arrays with low filling factor for enhanced infrared absorption. *J. Infrared Millim. Waves* **2021**, *40*, 1.
25. Choi, K.K.; Allen, S.C.; Sun, J.G.; DeCuir, E.A. Resonant detectors and focal plane arrays for infrared detection. *Infrared Phys. Technol.* **2017**, *84*, 94–101. [[CrossRef](#)]
26. Choi, K.K.; Dang, G.; Little, J.W.; Leung, K.M.; Tamir, T. Quantum grid infrared spectrometer. *Appl. Phys. Lett.* **2004**, *84*, 4439–4441. [[CrossRef](#)]
27. Zumukhorol, M.; Khurelbaatar, Z.; Kim, J.-H.; Shim, K.-H.; Lee, S.-N.; Leem, S.-J.; Choi, C.-J. Effect of a SiO₂ Anti-reflection Layer on the Optoelectronic Properties of Germanium Metal-semiconductor-metal Photodetectors. *J. Semicond. Technol. Sci.* **2017**, *17*, 483–491. [[CrossRef](#)]
28. Rosfjord, K.M.; Yang, J.K.; Dauler, E.A.; Kerman, A.J.; Anant, V.; Voronov, B.M.; Gol'tsman, G.N.; Berggren, K.K. Nanowire single-photon detector with an integrated optical cavity and anti-reflection coating. *Opt. Express* **2006**, *14*, 527–534. [[CrossRef](#)] [[PubMed](#)]
29. Andresen, B.F.; Ozaki, K.; Fulop, G.F.; Uchiyama, Y.; Nishino, H.; Matsukura, Y.; Kajihara, N.; Fujii, T. Development of mid-wavelength QWIP FPA. In Proceedings of the Infrared Technology and Applications XXXI, Orlando, FL, USA, 28 March–1 April 2005.
30. Besikci, C. Nature Allows High Sensitivity Thermal Imaging With Type-I Quantum Wells Without Optical Couplers: A Grating-Free Quantum Well Infrared Photodetector With High Conversion Efficiency. *IEEE J. Quantum Electron.* **2021**, *57*, 1–12. [[CrossRef](#)]
31. Pan, J.L.; Fonstad, C.G. Theory, fabrication and characterization of quantum well infrared photodetectors. *Mater. Sci. Eng. R Rep.* **2000**, *28*, 65–147. [[CrossRef](#)]